



# Differentiated Neogene bauxitization of volcanic rocks (western Cameroon): Morpho-geological constraints on chemical erosion

Mathieu Nouazi Momo<sup>a,\*</sup>, Anicet Beauvais<sup>b</sup>, Paul Tematio<sup>c</sup>, Martin Yemefack<sup>d</sup>

<sup>a</sup> Institute of Geological and Mining Research (IRGM), P.O. Box 4110, Yaoundé, Cameroon

<sup>b</sup> Aix-Marseille Univ, CNRS, IRD, INRAE, Coll France, CEREGE, BP 80, 13545, Aix-en-Provence, Cedex 4, France

<sup>c</sup> University of Dschang, Faculty of Science, Department of Earth Sciences, P.O. Box 67, Dschang, Cameroon

<sup>d</sup> International Institute of Tropical Agriculture (IITA), ASB Partnership REALU Project, P.O. Box 2008, Messa, Yaoundé, Cameroon

## ARTICLE INFO

### Keywords:

Bauxite  
Lateritic weathering  
Geochemical mass balance  
Chemical erosion  
Volcanic rocks  
Cameroon

## ABSTRACT

Lateritic weathering of Miocene volcanic rocks from western Cameroon highlands formed duricrusted bauxitic profiles. Two weathering profiles on ca. 14 Ma basalt and ca. 16 Ma trachyte were studied using geochemical mass balance functions. Less mobile elements Ti and Zr were used as references to quantify volumetric change (strain,  $\epsilon$ ), element transfer rate ( $\tau$ ) and geochemical mass transfers during the bauxitization process of basalt and trachyte. Conversion of parent rocks to kaolinite and goethite rich saprolites evolved to Al-Fe rich bauxites, mostly composed of gibbsite and iron oxy-hydroxides (goethite and hematite). However, formation of Al-Fe bauxitic profiles required higher Si leaching on trachyte than on basalt. Our results document that chemical weathering of a larger thickness of trachyte than basalt has been required to form a unit meter of weathering profile, implying differential rates of rock chemical erosion and topographic decay of landscapes. Rates of chemical erosion and formation of lateritic weathering profiles in western Cameroon have been mostly controlled by drainage conditions and volcanic rocks composition (mostly SiO<sub>2</sub> content differences), that also resulted in contrasted landscapes evolution during the Neogene.

## 1. Introduction

Lateritic regoliths of tropical shields generally have formed by long-term rock weathering under warm / humid and seasonally contrasted climates (Tardy, 1997). In tropical landscapes, lateritic paleosurfaces bearing bauxites and ferricretes have been relatively well preserved over geological times scale (Beauvais and Chardon, 2013). Formation of bauxite or ferricrete depends on climatic and morpho-tectonic conditions that control solute leaching processes and aluminum or iron accumulations in lateritic weathering profiles formed on erosional landforms (Bardossy and Aleva, 1990; Thomas, 1994; Valetton, 1999), including duricrusted Fe-cemented pediments (Chardon et al., 2018).

In Africa, bauxites have formed by intense lateritic weathering of various lithologies (Boulangé and Millot, 1988) mostly from ca. 59 to ca. 45 Ma (Beauvais et al., 2008) upon the African surface that extends from West to East and South-East Africa (Beauvais and Chardon, 2013; Burke and Gunnell, 2008; see also Perelló et al., 2020; De Putter and Ruffet, 2020). Likewise, thick bauxitic profiles later formed from weathering of 14 Ma to 23 Ma old trachyte and basalt are well preserved at altitudes of 1500 to 1800 m in the eastern Nigeria (Schwarz,

1997). With the mid-Miocene climatic optimum, Lateritic weathering intensified in Africa (e.g., Beauvais et al., 2008; De Putter and Ruffet, 2020), and more generally on continents of the inter-tropical belt (Retallack, 2010) even at relatively high altitudes, e.g., upon elevated continental margins (Jean et al., 2020), where transported-limited erosion regimes have potentially controlled landscapes evolution over the Cenozoic.

Previous studies established the geochemical variability of bauxitic profiles with regard to underlying parent rocks, as well as the link with local morphoclimatic conditions that prevailed during lateritic weathering, as exemplified in West Africa (Boulangé, 1984; Valetton and Beißner, 1986), Asia (Zarasvandi et al., 2012), Eastern Australia (Eggleton et al., 1987), Southern America (Boulangé and Colin, 1994; Soler and Lasaga, 2000; Soares de Oliveira et al., 2013), and India (Babechuk et al., 2014). Chemical weathering of basalt and volcanic rocks has been recently considered into the frame of major surface processes that govern the Critical Zone (Brantley and Lebedeva, 2011; Babechuk et al., 2015; Wille et al., 2018).

In situ formed bauxitic profiles are suitable to quantify geochemical mass transfers during long-term rock weathering. Since the pioneering

\* Corresponding author.

E-mail address: [nouazimat@yahoo.fr](mailto:nouazimat@yahoo.fr) (M.N. Momo).

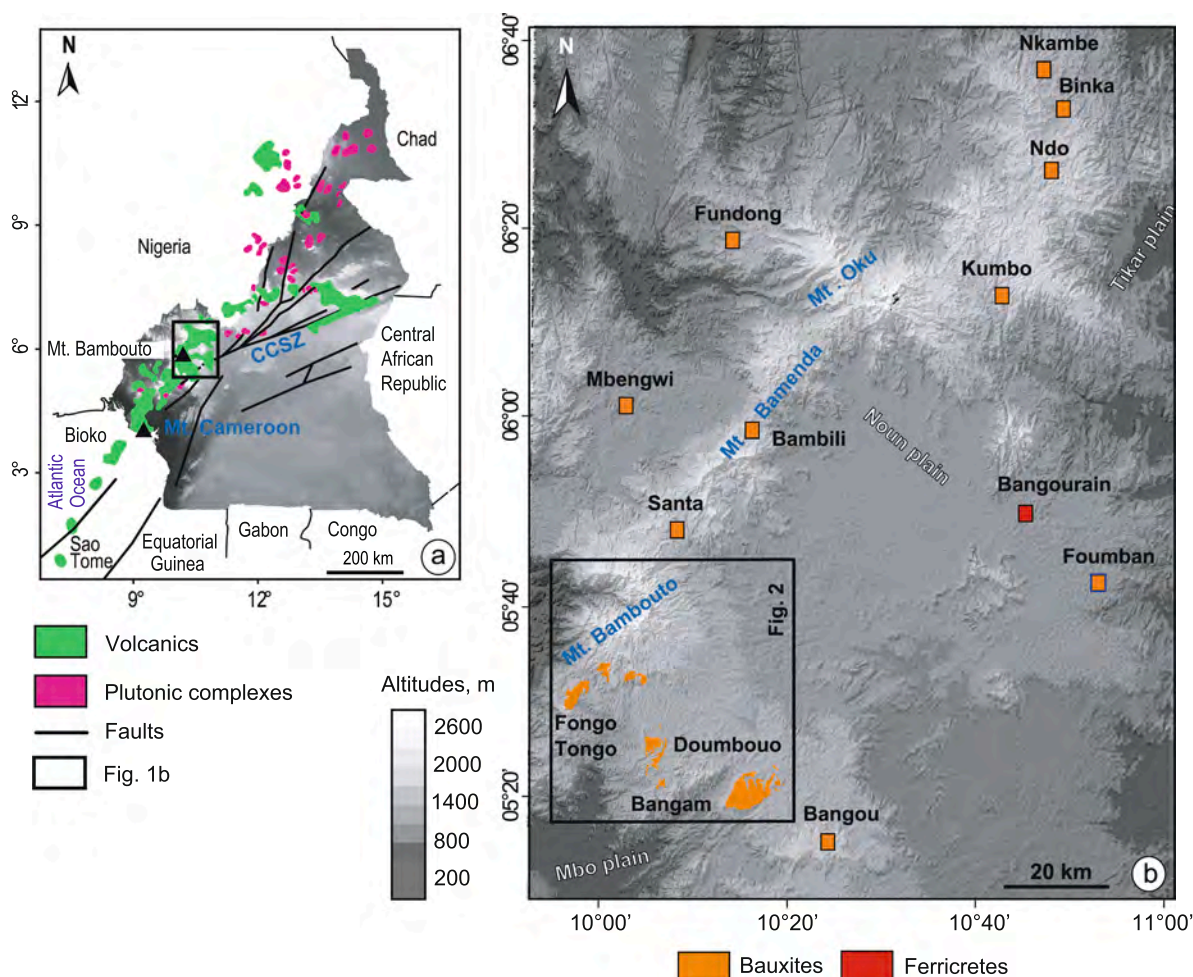


**Fig. 1.** a) Location of the Western Cameroon Highlands. The main geological features (Adapted from Nkouathio et al., 2008) are superimposed to the digital elevation model of Cameroon. CCSZ = Central Cameroonian shear zone; b) Morphology of the Western Cameroon Highlands and location of the study area with main occurrences of bauxite and ferricrete bearing surfaces.

introduction from Millot and Bonifas (1959), and mathematical formalization by Brimhall and Dietrich (1987) and Brimhall et al. (1988), the geochemical mass balance approach was commonly used for quantifying the accumulation or depletion of major and trace elements during weathering processes (e.g., Colin et al., 1992; Beauvais and Colin, 1993; Braun et al., 1993; Tematio and Olson, 1997; Temgoua et al., 2003, among others). However, few studies have addressed elemental geochemical mass balance of lateritic bauxitic profiles (e.g., Boulangé and Colin, 1994; Eggleton et al., 2008). In western Cameroon region and on the Adamaoua plateau above the Central Cameroonian shear zone (CCSZ, Fig. 1), bauxitic regolith formed on high altitude surfaces (up to ~ 1900 m) from lateritic weathering of mid- to lower Miocene volcanic rocks of the Cameroon volcano-tectonic line. Here, we have quantified element mass transfers (gains and losses of major chemical elements) in lateritic weathering profiles formed upon mid-Miocene basalt and trachyte from the western highlands of Cameroon. Our results document differential morpho-geological controls on the rate of rock chemical erosion, formation of bauxitic regolith and landscapes evolution in western Cameroon over the Neogene.

## 2. Geological and morphological setting

In the western highlands of Cameroon, wide Cenozoic volcanic complexes (e.g. Mounts Bambouto and Bamenda; Fig. 1) including mafic and felsic plutons have been extruded through the Neoproterozoic granito-gneissic basement (Kwékam et al., 2010). Tertiary to

recent strato-volcanoes culminate up to 3000 m a.s.l., above low-relief lateritic landsurfaces and grabens (Déruelle et al., 2007; Nkouathio et al., 2008), i.e., Mbo (ca 700 m a.s.l.), Noun (ca 1100 m a.s.l.) and Tikar (ca 750 m a.s.l.) plains (Fig. 1b).

Volcanic activity has begun in Cameroon from the Eocene with the early establishment of the Bamoun plateau between 51.8 and 46.7 Ma (Moundi et al., 2007) and Mount Bangou between 44.7 and 43.1 Ma (Fosso et al., 2005). Peaks of magmatic activity also generated (1) Oligo-Miocene basaltic flows (31 to 14 Ma) of little differentiated silicic magmas from an asthenosphere source, and (2) most evolved Mio-Quaternary (15 Ma to 4 Ma) silicic magmas from amphibole bearing lithospheric mantle source (Marzoli et al., 1999; Marzoli et al., 2000).

Between longitudes 09°50" and 11°00" and latitudes 05°10" and 06°40" (Fig. 1b), volcanic rocks have been intensively weathered since mid-Miocene. Studied lateritic weathering profiles are mostly bauxitic and formed upon trachyte of ca. 16 Ma at Fongou Tongo and on basalt of ca. 14 Ma at Doumbouo (Nkouathio et al., 2008) in the southernmost part of the western Cameroon highlands (Fig. 1b and Fig. 2). Sparse pre-Neogene lateritic profiles topped by ferricretes also overly gneissic basement.

On trachyte around Fongou Tongo (Fig. 2a-b), a low-relief lateritic landscape with smooth hilly landforms at altitudes ranging from ca. 1570 m to ca. 1650 m is drained by a first order dense alveolar drainage network ca. hundred meters meshed, and bounded by incisions of ca. 150 m to ca. 200 m deep from West to East (Fig. 2a-b and Fig. Supplementary figure 1 DR1a). On basalt near Doumbouo (Fig. 2b),

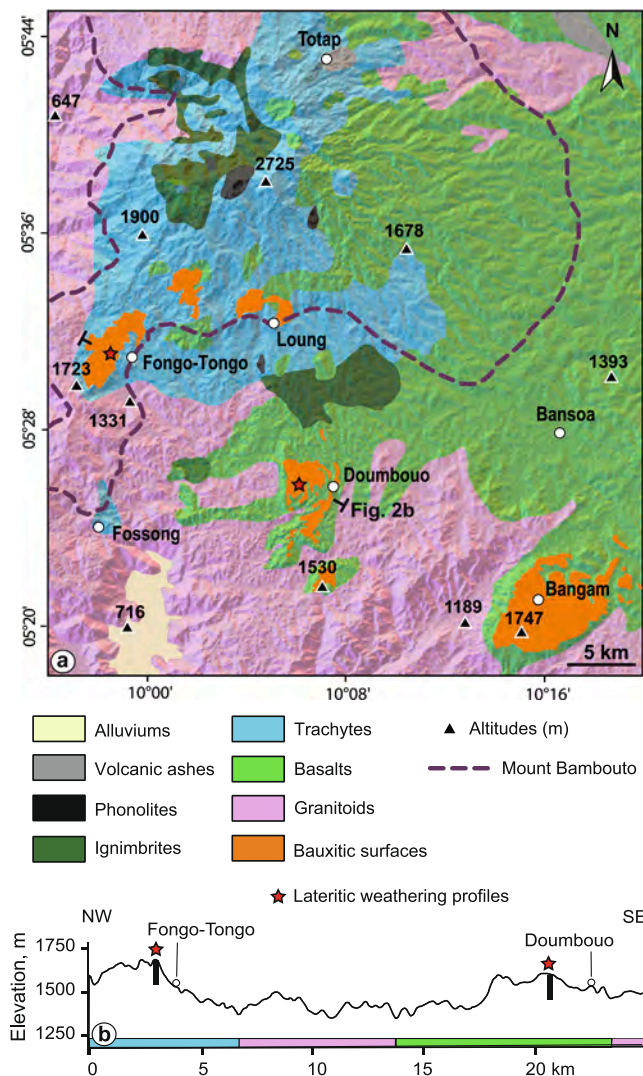


Fig. 2 (Catena10553)

Fig. 2. a) Geological map of the Western Cameroon Highland with main bauxitic surfaces (Bamileke plateau, see insert in Fig. 1b). b) Morpho-geological section showing the topographic location of studied bauxitic profiles on trachytes and basalts. See section trace on Fig. 2a.

relatively flat lateritic plateaus at altitudes between ca. 1545 m to ca. 1585 m are drained by a first order linear drainage network and incised from ca. 100 to 120 m deep (Fig. 2b and Fig. Supplementary figure 1 DR1b). High altitude grasslands cover the two landscapes that are both subject to sub-equatorial climate (Kengni et al., 2009) with ~ 1600 mm mean annual rainfall and 18.1 °C of mean annual temperature.

### 3. Materials and methods

Two pits were dug through thick lateritic mantles representative of the two landscapes (Fig. 2), on the basis of a previous geomorphological study in the region (Momo Nouazi et al., 2016). The first profile (5° 31' 51.16"N / 9° 58' 34.99"E) formed upon trachyte at Fongo-Tongo, while the second one (5° 25' 19.36"N / 10° 05' 46.98"E) formed upon basalt at Doumbouo (Fig. 2a-b; see also Figs. DR1a-b). After detailed macroscopic descriptions along side pits walls, twenty samples (~2 kg) representative of ca. one cubic meter in the different horizons of profiles were collected based on their petrographic structures. Fresh trachyte was sampled in nearby quarry excavation, and basalt under the saprolite of its weathering profile.

Petrographic studies were carried out on thin sections of fresh rocks and weathered samples to describe textures of weathering products and their mineral composition. Samples were crushed to a sieve size < 63 µm for mineralogical and geochemical analysis. Mineralogical analyses were performed using XRD (X-Ray Diffractometry), with an X'Pert Panalytical diffractometer using CuKα radiation (1.79 Å) in the range of 2° to 78° 2θ and at a speed of 0.2°/min (10 s counting time every 0.033°). Minerals were identified upon diffraction spectra using High Score X'Pert Plus software (Version 3.0) and compared with known standards (American Mineralogist Crystal Structure Database, 2017). A Rietveld Refinement process (Rietveld, 1969; Ufer et al., 2008) was also applied for semi-quantifying the proportion (%) of each mineral. Each Mineral proportion is obtained by the ratio between the surface areas of specific XRD peaks of each mineral to the total surface of the sample XRD pattern. Geochemical analyses were obtained using ICP methods from pulverized samples fraction. Major and trace elements were analyzed by ICP-AES (Inductively coupled plasma-Atomic emission spectrometry).

#### 3.1. Element mass transfer functions

The element mass transfer function (Brimhall and Dietrich, 1987) was applied as it accounts for the chemical composition and bulk density of weathered horizons and parent rocks, allowing to estimate the porosity and volume change or strain ( $\epsilon$ ) across the weathering profile. This function also requires a reference element, which is generally included in resistant minerals and considered as less mobile during weathering. The reference elements commonly used are Zr, Ti, and Th (Brimhall and Dietrich, 1987; Beauvais and Colin, 1993; Boulangé and Colin, 1994; Braun et al., 1993; White et al., 2001; Tematio et al., 2009). Finally this mass transfer function allows quantifying the accumulation or depletion of elements during weathering.

Physical parameters of weathering horizons are first measured to establish:

$$\phi = 1 - \frac{\rho_b}{\rho_g} \quad (1)$$

$\phi$  is the porosity, while  $\rho_b$  and  $\rho_g$  in  $\text{g.cm}^{-3}$  refer to bulk density and grain density of each sample representative of a given weathering horizon. Bulk density,  $\rho_b$ , of dried samples was estimated after weighing and coating them with molten paraffin wax, followed by their immersion in water to measure displaced volume. Grain density,  $\rho_g$ , was measured using water picnometer. Both densities were measured with an accuracy of  $\sim \pm 1\%$ .

Strain,  $\epsilon$ , is then defined by:

$$\epsilon_{i,w} = \frac{\rho_b \times C_{i,p}}{\rho_g \times C_{i,w}} - 1 \quad (2)$$

where  $i$  refer to the element considered as the less mobile during weathering,  $\rho$  is the bulk density and  $C$  the concentration of the reference element in g/100 g in weathered sample ( $w$ ) and parent rock ( $p$ ). Measurement of strain,  $\epsilon$ , allows quantification of the volumetric change across weathering profile owing to its collapse (Brimhall and Dietrich, 1987; see also Chadwick et al., 1990).

Then, transfer rate,  $\tau$ , (gain or loss) of a mobile element  $j$  either by relative or absolute accumulation (including physical translocation) or solute depletion is defined from:

$$\tau_{j,w} = \left[ \frac{\rho_w \times C_{j,w}}{\rho_p \times C_{j,p}} \times (\epsilon_{i,w} + 1) \right] - 1 \quad (3)$$

Quantification of the mass of element  $j$ ,  $m_{j,w}$ , in  $\text{kg/m}^3$  transferred through a unit volume ( $1 \text{ m}^3$ ) of profile during both saprolite formation and bauxitization can also be obtained by:

$$m_{j,w} = \left( \frac{C_{j,p}}{100} \times \rho_p \times V_p \right) \times \tau_{j,w} \quad (4)$$

The total mass of element  $j$ ,  $M_{j,w}$  in kg, transferred through a cross section of weathering profile during the chemical weathering of a given height or thickness of parent rock is derived by integrating  $\tau_{j,w}$  as a function of depth. However, knowledge of initial height  $z$  of parental rock (or protolith layer thickness) that has been chemically weathered to form the investigated profile of thickness  $\Delta z_w$  is required. According to Egli and Fitze (2000) this is obtained by relating  $\Delta z_w$  to  $\Delta z$  using the strain,  $\varepsilon_{i,w}$ , such as:  $\Delta z = \Delta z_w (1/\varepsilon_{i,w} + 1)$ . Therefore, the higher is  $\varepsilon_{i,w}$  the higher is the thickness of protolith layer that has been chemically weathered to form a given profile. The masses of elements  $M_{j,w}$  (gain or loss) transferred through each profile horizon during the chemical weathering of a corresponding thickness of parent rock is then integrated upon the total profile depth,  $D$ , as established by Egli and Fitze (2000):

$$M_{j,w} = \left( \frac{C_{j,p}}{100} \times \rho_p \right) \times \left( \frac{1}{\varepsilon_{i,w} + 1} \right) \times \int_{z=0}^{z_w=D} \tau_{j,w} \times dz_w \quad (5)$$

## 4. Results

### 4.1. Lateritic weathering on trachyte

Trachyte outcrops on steep slopes and in talwegs, and is deeply weathered with bauxite formed on top of flat to gently sloping interfluvies. Trachyte has a microlitic texture with no or few porphyric minerals (Fig. 3a), and made up of an assemblage of microcrystalline plagioclases (Pl), clinopyroxenes (cpx), Fe-Ti oxides, and scarce Cpx phenocrysts (up to 1 mm) (Fig. 3b and 3c). These minerals also include anorthoclase ( $\text{An}_{25-11}\text{Ab}_{70-54}\text{Or}_{22-19}$ ) and alkali feldspars, i.e., sanidine to Na-sanidine ( $\text{Or}_{15-55}\text{Ab}_{35-85}\text{An}_{0-6}$ ), sodic Cpx ( $\text{En}_{3-4}\text{Aeg}_{33-35}\text{Fs}_{62-65}$ ) or hedenbergite ( $\text{Wo}_{45-47}\text{En}_{26-30}\text{Fs}_{40-44}$ ) and titanomagnetite (94–25 mol% ulvöspinel) (see Nkouathio et al. 2008).

Lateritic bauxitic profiles have been formed in-situ on trachyte, whose the structure is coarsely preserved in saprolite, but transported materials may also be reworked on pediments established around the bauxitic hilly landforms at lower altitudes (See Momo Nouazi et al., 2019). The weathering profile includes a saprolite (C), a blocky bauxitic duricrust (B5), a massive bauxitic duricrust (B3) and a loose nodular

bauxitic horizon on top (B1) (Fig. 4a, see Momo Nouazi et al., 2019). The saprolite is porous (Tab. 1), with inter-connected voids resulting from eluviation process of less cohesive clays (Fig. 5a). It is made up of a grey brown matrix of kaolinite and gibbsite (61% and 16%, respectively), and it also contains goethite formed by pseudomorphosis of Px, Cpx and Fe-Ti oxides, and some anatase and maghemite. The horizon B5 shows decimeter-size blocks of porous reddish bauxitic duricrust mixed with centimeter size nodules embedded in a loose matrix. Compared to saprolite, the mineralogical composition (Table DR1a, see Momo Nouazi et al., 2019) shows a total conversion of kaolinite into gibbsite (57%), and goethite coating/infilling (29–58%) in bauxitic blocks. The massive bauxite duricrust is made up of a reddish brown matrix mixing gibbsite (up to 68%) and goethite (up to 33%) and preserving some residual features of parent minerals (e.g. pyroxene). It is crossed by micrometer to millimeter voids coated with thick Al- and Fe-rich accumulations (Fig. 5b), while showing centimeter size sub-horizontal laminated iron cementations at its bottom (Fig. 4a). The surface horizon (B1) is made up of a loose matrix embedding fragments of bauxite duricrusts and bauxitic nodules whose petrographic structures are quite similar to that of the underlying massive bauxite. The horizon B1 has more kaolinite (22%) than the massive bauxite (B3) and less gibbsite and goethite (31 and 18%, respectively), with up to 18% of quartz of detrital origin.

Main geochemical trends highlight relative enrichment of  $\text{Al}_2\text{O}_3$ ,  $\text{Fe}_2\text{O}_3$ , compared to parental trachyte (Fig. 4a and Fig. 6), while  $\text{SiO}_2$  with alkaline/alkaline-earth elements are depleted (see also Table DR2a, and Momo Nouazi et al., 2019). Noted that locally soils and upper parts of profiles formed also on trachyte from the same area (Tematio et al., 2009) may be more siliceous but less rich in  $\text{Al}_2\text{O}_3$  and/or  $\text{Fe}_2\text{O}_3$  than our samples (Fig. 6). The  $\text{SiO}_2$  content decreases from the trachyte (59.5 wt%) to its minimum content in the massive bauxitic duricrust (0.73 wt%), and increases toward the surface to 19.25 wt% (Fig. 4a). The  $\text{Al}_2\text{O}_3$  and  $\text{Fe}_2\text{O}_3$  contents increase from the trachyte (15.5 wt% and 8.4 wt%) to their maximum contents in the massive bauxite duricrust (51.8 wt% and 25.9 wt%), respectively, and then decrease toward the surface (Fig. 4a). Note the increase in  $\text{Fe}_2\text{O}_3$  and decrease in  $\text{Al}_2\text{O}_3$  at the transition between B3 and B5 horizons where ca. 1 m thick iron rich accumulations occurred (Fig. 4a). The  $\text{TiO}_2$  content increases from 0.62 wt% in the trachyte to 3.39 wt% in the massive bauxitic duricrust, while  $\text{P}_2\text{O}_5$  increases in the saprolite and then slightly decreases in the upper duricrusted bauxitic horizons

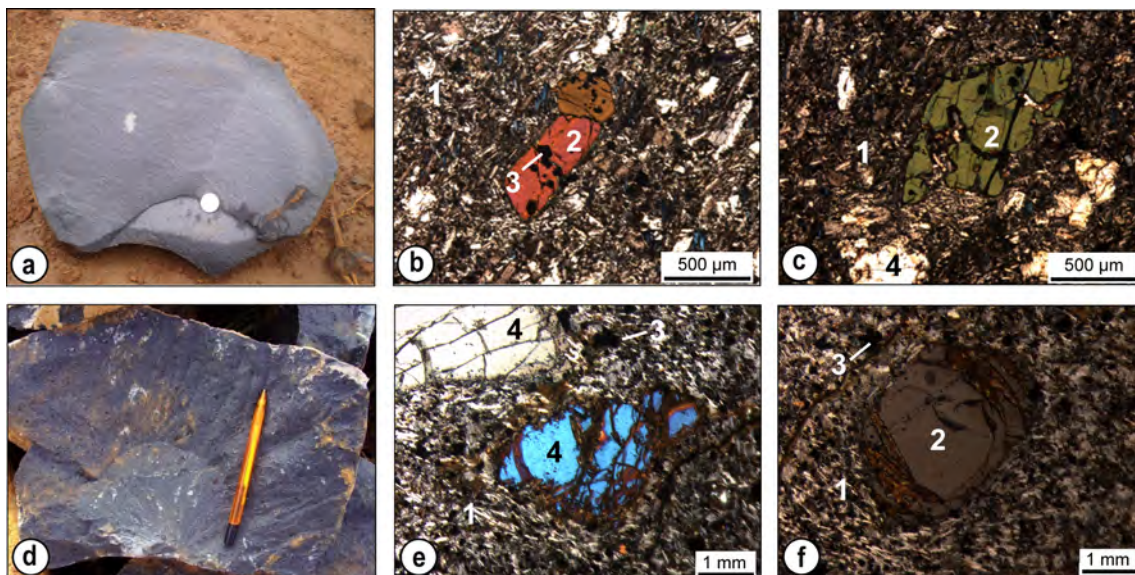


Fig. 3. a) Macroscopic view of trachyte sample; b and c) Crossed-polarized microscope photomicrographs of the porphyritic trachyte. d) Macroscopic view of basalt sample; d) and e) Crossed-polarized microscope photomicrographs of the porphyritic basalt. 1 = plagioclases; 2 = olivine; 3 = titanomagnetite; 4 = clinopyroxenes.

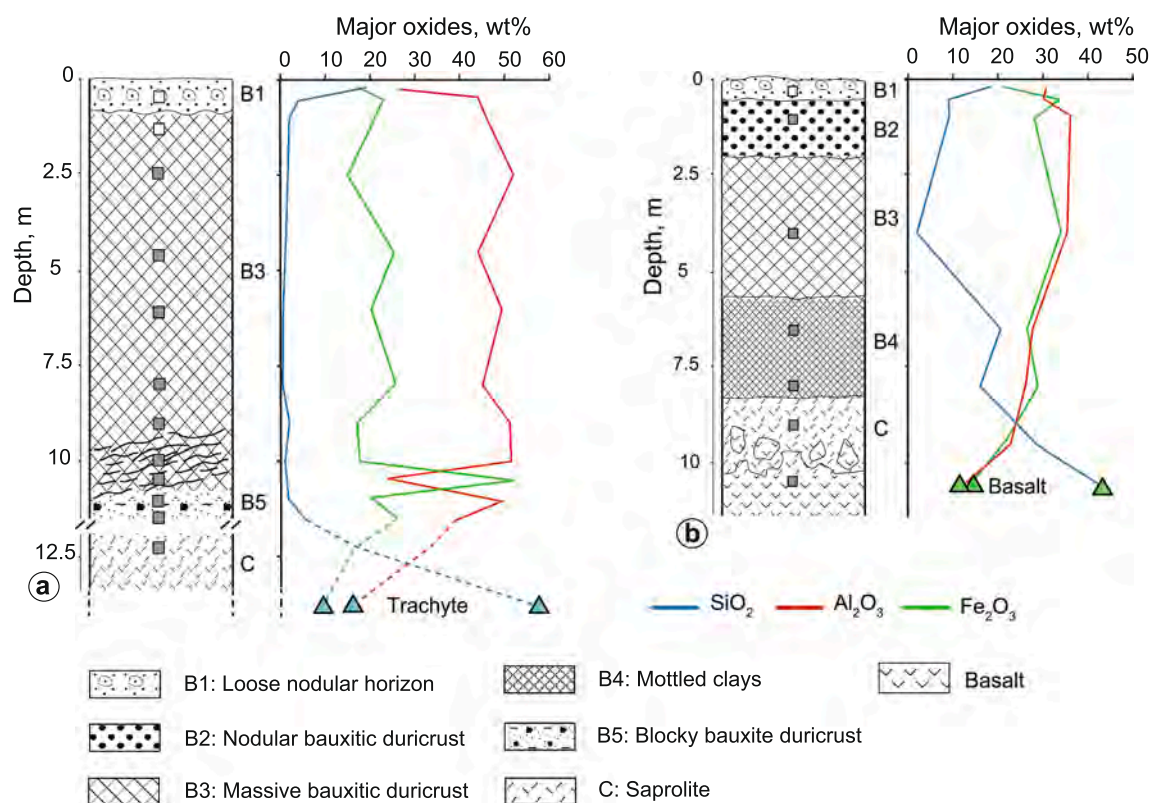


Fig. 4. Petrographic structures, location of samples collected (squares), and variations of major oxides content in weathering profiles formed on a) trachyte, and b) basalt. Grey squares = samples analyzed for mass transfer balance.

(Fig. 7a and Table DR2a). Along the profile, trace elements, Nb, Zr, Ga, Cu, Ni, Co, Cr, V, As, Pb, Th, Hf, U and Ta contents are higher, while Y, Sr, Rb, contents are lower than those in trachyte (see also Momo Nouazi et al., 2019 for more details; and Tab. DR3a).

#### 4.2. Lateritic weathering on basalt

Porphyritic basalt is deeply weathered and occurs as boulders on slopes. Phenocrysts are clearly identified on field samples (Fig. 3d), and represent up to 30% of the sample (Fig. 3e and 3f). Parent minerals of this basalt also include large olivine (Fo<sub>66-87</sub>), diopsides (Wo<sub>45-48</sub>En<sub>43-52</sub>Fs<sub>8-17</sub>), augites (Wo<sub>38-44</sub>En<sub>43-53</sub>Fs<sub>10-23</sub>), scarce phenocrysts and microcrystalline plagioclases (An<sub>46-72</sub>) and Fe-Ti oxydes (71–19 mol% ulvöspinel) (see Nkouathio et al. 2008).

The lateritic profile is located on top of a flat interfluvium limited by incisions (Fig. 2b and Fig. DR1b). From the bottom to the top, the profile includes a saprolite (C), a mottled-clays layer (B4), a massive bauxitic duricrust (B3), a nodular bauxitic duricrust (B2) and a loose nodular horizon on top (B1) (see Fig. 4b). The saprolite is more porous than on trachyte (Tab. 1), and composed of a greyish-brown kaolinite matrix (57%) dotted with residual porphyritic olivines/pyroxenes. It is studded by millimeter sized dissolution voids preserving the original shapes of ol and cpx phenocrysts (Fig. 5c). It also shows dark-brown goethite (30%) and maghemite (9%). The mottled-clays have lost the basalt structure and are composed of a brown argillic frame of kaolinite (46%), goethite (24%), and minor amount of maghemite (5%); the mottled clays also have centimeter size gray volumes of microcrystalline gibbsite (18% of the total horizon), and Al-Fe cutans fillings voids and cracks. The structure of the massive bauxitic duricrust is quite similar to mottled-clays, but the brown argillic plasma bears microcrystalline gibbsite. Clay-ferruginous materials refill voids and later differentiate into Fe-rich cutans (Fig. 5d). The bulk mineral composition of this bauxitic duricrust shows lesser kaolinite (4%) than mottled-clays, more gibbsite (41%) and goethite (27%) and up to 15% hematite

(see also Table DR1b). Centimeter size nodules of the nodular bauxitic duricrust represent 75% of the horizon. They are composed of a brown argillic matrix of goethite and kaolinite locally preserving the basalt structure and are rimmed with millimeter size dark brown cortex. The reddish inter-nodular matrix is mostly composed of goethite and microcrystalline gibbsite filling millimeter size cracks. The bulk mineral composition of the horizon shows more kaolinite (10%), gibbsite (46%) and goethite (38%), but lesser hematite (> 5%) than the massive bauxite duricrust. The surface nodular horizon (B1) is composed of a mixture of fine earth and centimeter size nodules, with an internal structure similar to that of massive and nodular duricrusts. Kaolinite content increases to 15%, while gibbsite and goethite decrease to 35 and 23%, respectively (Table DR1b). However, this horizon contains also up to 15% quartz, which is probably, as on profile of trachyte, of detrital origin.

Main geochemical trends first show higher Al<sub>2</sub>O<sub>3</sub> and Fe<sub>2</sub>O<sub>3</sub> compared to basalt, while SiO<sub>2</sub> is depleted from the profile (Fig. 4b and 6), with P<sub>2</sub>O<sub>5</sub> and alkaline/alkaline-earth elements (see Table DR2b). The SiO<sub>2</sub> content decreases from the basalt (42.0 wt%) to its minimum content in the massive bauxitic duricrust (1.77 wt%), and increases toward the surface to 18.35 wt% (Fig. 4b). The Al<sub>2</sub>O<sub>3</sub> and Fe<sub>2</sub>O<sub>3</sub> contents increase from the basalt (13.0 and 14.25 wt%) to maximum contents in the duricrusted horizons (36.0 and 34.2 wt%), respectively, and then decrease toward the surface (Fig. 4b). The TiO<sub>2</sub> content also increases from 3.69 wt% in basalt to 8.83 wt% in the mottled clays (Fig. 7a and Table DR2b). Compared to basalt, trace elements Sc, V, Cr, Zn, Ga, Zr, Nb, Hf, Ta, Pb, Th and U have higher contents, while Ni, Cu, As, Rb, Sr, Y and Ba contents are lower along the profile (see Tab. DR3b).

#### 4.3. Element mass transfers during weathering and bauxitization

Because samples from the upper part of profiles may integrate some reworked materials of potentially allochthonous origin (e.g., colluvia),

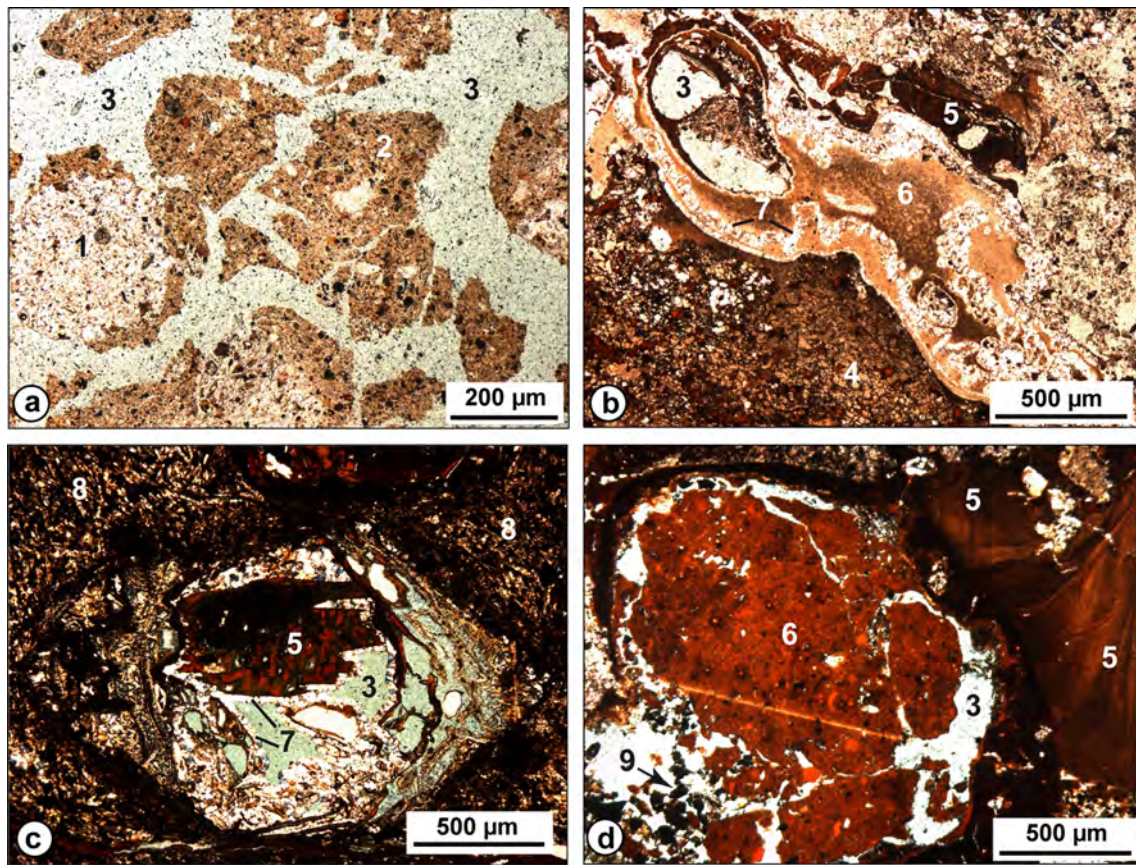


**Fig. 5.** Transmitted natural light microscopic photomicrographs of a) sapolite and b) bauxitic duricrusts from lateritic profile on trachyte; and from lateritic profile on basalt, c) sapolite showing weathering of primary plagioclases and cpx phenocrystal; and d) bauxitic duricrust. 1 = primary gibbsite crystallizations; 2 = Ferruginous argillic matrix; 3 = void; 4 = primary gibbsite with Fe-coating; 5 = goethite rich Fe clay cutan; 6 = Clay ferruginous infill; 7 = secondary gibbsite crystallizations; 8 = gey-argillic matrix with primary gibbsite and Fe-coating; 9 = translocated heavy minerals.

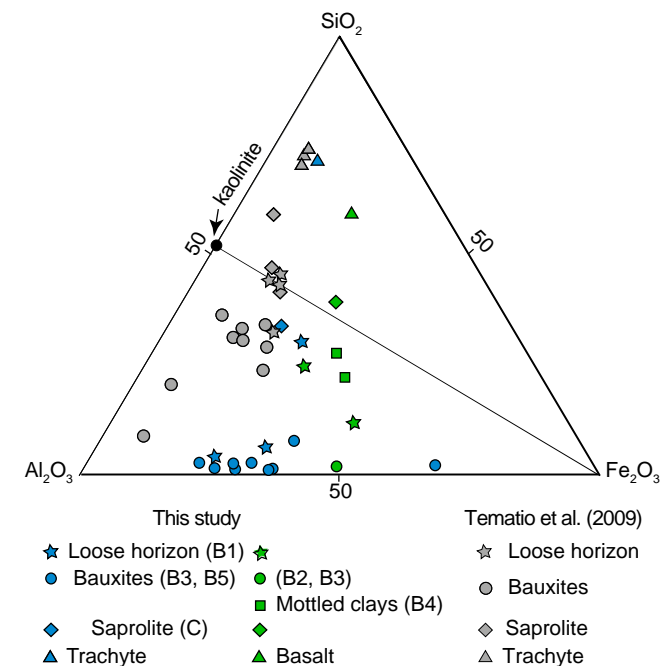


**Fig. 6.** Major oxides composition of parent rocks, sapolite and duricrusted horizons in profiles formed on trachyte and basalt.

which include detrital quartz and anomalous silica content (Fig. 6; see also Tables DR1 and DR2) and possibly detrital heavy minerals (ex: zircon on basalt, Fig. 7a), mass balance calculations have been only applied on ten and five samples in the profiles formed in-situ on trachyte and basalt, respectively (Fig. 4).

4.3.1. Characterization of reference elements

Reference elements, Zr and Ti, are characterized by their relatively low mobility during bauxitization. Their distribution across the weathering profiles compared to their amount in parent rocks allows documenting changes in chemical and physical processes in different horizons of profiles. Here, Zr and Ti show a differentially correlated distribution across the weathering profiles (Fig. 7a), as previously observed by Schwarz (1997) and Tematio et al., (2009) in comparable morphogeological settings (Fig. 7b). The distributions of Zr and Ti in the different profiles are comparable (Fig. 7a-b). These two elements show parallel behavior along the profiles (Fig. 7c), but Zr varies less than Ti on trachyte, while Ti is better expressed than Zr and most stable on basalt (Fig. 7d and 7e). However, departures from stoichiometric distributions owe to possible physical enrichments of Ti and Zr bearing-heavy minerals in different horizons of profiles (Fig. 7a and 7b).

Despite this, trachyte petrologic pattern is coarsely preserved in different horizons, although eluviation processes produce 20% to 30% porosity while illuviation forms secondary crystallizations of gibbsite and clay-Fe cutans cementations in duricrusted horizons (see Fig. 5). This results in grain density  $\rho_g$  of weathering samples close to that of the

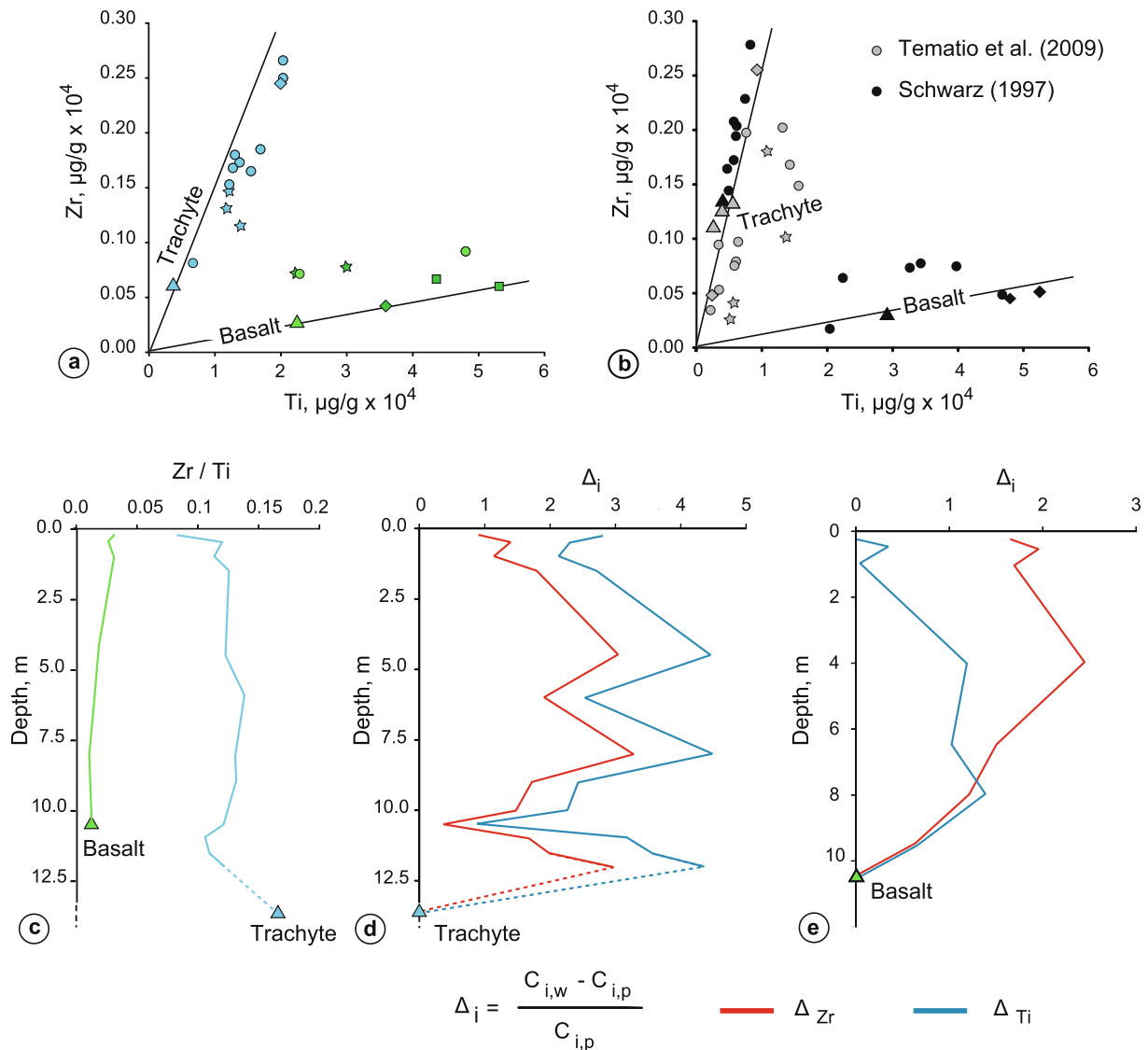


**Fig. 7.** Variations in the content of reference elements Zr and Ti in weathering profiles formed on trachyte and basalt. a) and b) Diagrams Zr vs. Ti (see Fig. 6 for explanations of symbols; Black straight lines indicate stoichiometric distributions); c) Zr/Ti vertical variations along both profiles; Zr and Ti variations along profile on d) trachyte, and e) basalt.

fresh trachyte (see Tab. 1a and Fig. 8a-b). These physical changes are all indicative of noticeable volumetric variations across the profile (Fig. 8c; see also Tab. 1). However, the overall variation of  $\varepsilon_{Zr}$  is  $\sim 13\%$  less than that of  $\varepsilon_{Ti}$ , with a mean value of  $-51\%$  (against  $-64\%$  for  $\varepsilon_{Ti}$ ) in the profile (Fig. 8c), supporting that Zr is the best reference element for mass balance calculations on trachyte. On the other hand, in the profile on basalt where porosity may increase to ca. 40% (Fig. 9b),  $\varepsilon_{Ti}$  varies much less than  $\varepsilon_{Zr}$  (Fig. 9c) and a better correlation between volumetric change  $\varepsilon_{Ti}$  and measured physical parameters validate Ti as most suitable reference element for mass balance calculation in the profile on basalt (see Table. 1b and Fig. 9d).

In the next sections, the element mass transfers involved during formation of the two weathering profiles are reported in the tables 2 and 3 and synthesized in the Fig. 10. The table 2 reports masses ( $m_{j,w}$ ) of elements transferred through a unit volume (1 m<sup>3</sup>) calculated from eq. (4). The table 3 shows masses transferred  $M_{j,w}$ , of these elements calculated from eq. (5), and integrated over the investigated profiles depth related to the corresponding height or thickness of chemically weathered rock.

#### 4.3.2. Element mass transfers in weathering profile on trachyte

Ti shows a transfer rate of 35% in the saprolite relative to the trachyte (Tab. 1a and Fig. 8d) that results in 3.3 kg/m<sup>3</sup> or 11 kg of Ti concentrated in 1.5 m thick saprolite (Tab. 2a and 3a, and Fig. 10a). Above the saprolite, the blocky bauxite (B5) and the massive bauxite (B3) horizons together show transfer rates of Ti from 21% to 56% that corresponds to ca. 2 to 8 kg/m<sup>3</sup> (Table 2a), or ca. 64 kg of Ti concentrated in ca. 10 m thick bauxitic duricrusted horizons (Table 3a and Fig. 10a). Al is depleted by 44% in the saprolite (Tab. 1a; Fig. 8d), corresponding to ca. 92 kg/m<sup>3</sup> or ca. 308 kg of Al exported from 1.5 m thick saprolite (Tabs 2a and 3a, and Fig. 10a). However, during formation of lateritic bauxitic duricrusts, the transfer rate of Al ranges from  $-33\%$  to  $+35\%$  corresponding to transferred mass of ca.  $-68$  to  $+72$  kg/m<sup>3</sup> (Tabs. 1a-2a), resulting in concentration of ca. 147 kg Al integrated over ca. 10 m thick lateritic profile (Tab. 3a and Fig. 10a). Fe is also depleted by 48% in the saprolite (Tab. 1), with a loss of  $-72$  kg/m<sup>3</sup> implying that ca. 240 kg of Fe is released during the formation of 1.5 m thick saprolite (Tabs. 2a and 3a and Fig. 10a). The transfer rate of Fe ranges from  $-40\%$  to  $+97\%$  in the bauxitic duricrusts

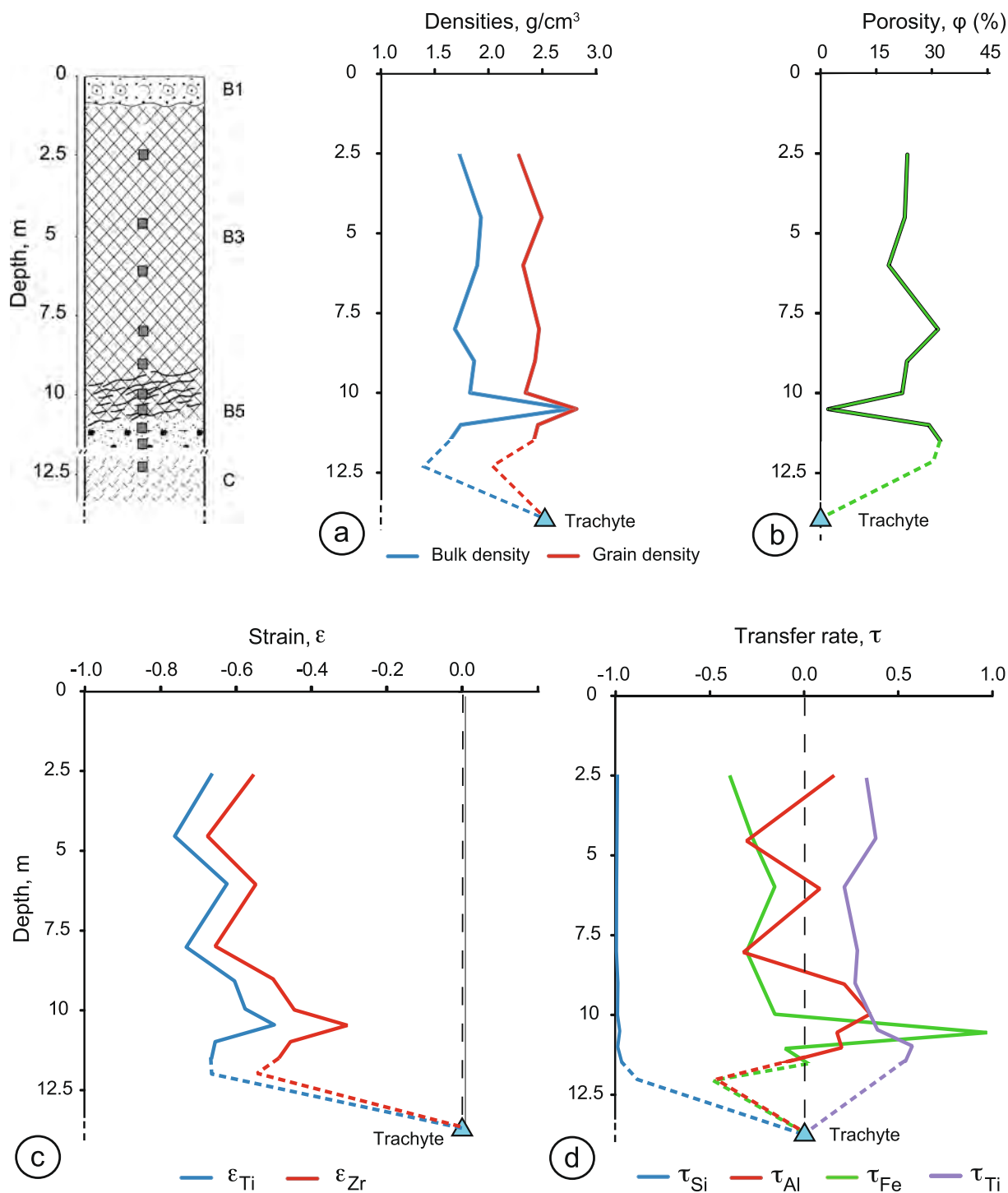


Fig. 8. Variation of physical parameters along the profile on trachyte. a) Densities; b) Porosity; c) Strain; and, d) Transfer rates of major elements.

corresponding to transferred masses of  $-58$  to  $+144 \text{ kg/m}^3$  and at least ca.  $708 \text{ kg Fe}$  exported by the formation of  $10 \text{ m}$  thick bauxitic duricrusted profile, despite concentration of ca.  $140 \text{ kg/m}^3$  at the base of duricrusted horizons (Tab. 2a and 3a and Fig. 10a).

In summary, Ti is the most enriched element in the trachyte profile, followed by Al, while Si, and P are the most depleted elements along the profile (Tab. 1a; Fig. 8d). Formation of  $1.5 \text{ m}$  thick saprolite resulted in export of a total mass of ca.  $2084 \text{ kg}$  of Si at a rate of  $-625 \text{ kg/m}^3$ , while a mass of ca.  $15898 \text{ kg}$  was exported by formation of  $10 \text{ m}$  thick lateritic duricrusted horizons (Tab. 2a and Fig. 10a). Mass changes calculation of trace elements highlights enrichment of V, Co, Ni, As, Nb,

Hf, Ta, Pb, U and Th, while Ba, Ga, Y, Sr, and Rb are depleted. Compared to major elements, their exported/accumulated masses are very low, with mean values of  $\pm 0.001$  to  $0.1 \text{ kg}$ , except Ba released up to  $-141 \text{ kg}$  (see Tab. DR4a).

#### 4.3.3. Element mass transfers in weathering profile on basalt

Al is gradually enriched throughout the profile from  $6\%$  in the saprolite to  $134\%$  integrated in lateritic horizons (B2 + B3 + B4), despite slight depletion of  $16\%$  in the mottled clays (Tab. 1b; Fig. 9d). This corresponds to ca.  $20 \text{ kg Al}$  concentrated in ca.  $2 \text{ m}$  thick saprolite (C) at a rate of  $11 \text{ kg/m}^3$ , while ca.  $680 \text{ kg}$  of Al concentrated in ca.  $8 \text{ m}$  thick

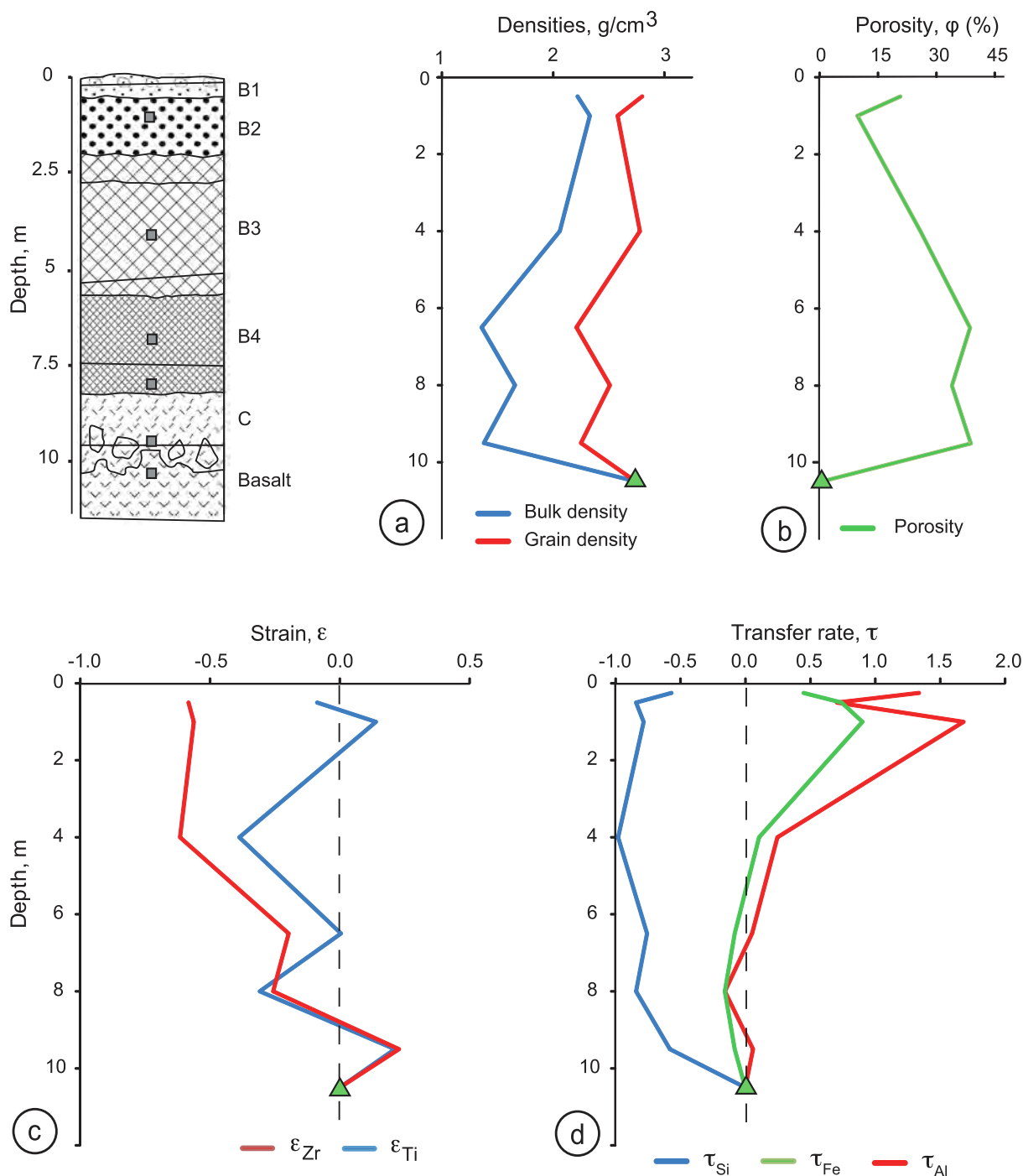


Fig. 9. Variation of physical parameters along the profile on basalt. a) Densities; b) Porosity; c) Strain; and, d) Transfer rates of major elements.

lateritic horizons (Tabs. 2b and 3b and Fig. 10b). Fe is depleted by 8% to 16% in the saprolite and the mottled clays, respectively, and enriched up to 90% in the nodular bauxite (Tab. 1b; Fig. 9d). These result in ca. 41 kg of Fe exported during saprolite formation at a rate of 22.5 kg/m<sup>3</sup>, while a total mass of ca. 414 kg of Fe concentrated in bauxitic lateritic horizons (Tabs. 2b and 3b, and Fig. 10b).

In summary, Al is the most enriched element in the basalt profile, followed by Fe, while Si, Mn and P are mostly depleted (Tabs. 2b and 3b; Fig. 9d and 10b). Si is strongly leached with a total mass of ca. 570 kg exported by the formation of 2 m thick saprolite, while 4867 kg of Si has been released by that of 8 m thick duricrusted lateritic horizons (Tab. 3b and Fig. 10b). The overall mass changes in trace elements show depletions in Rb, Sr, Y, Ba and transition elements, Co, Ni,

Cu and Zn along the profile, while Nb, Zr, Ga, Cr, V, Th, Hf, U and Ta are enriched in the upper 6 m of profile (Tab. DR4b). Most mass transfer values are very low except that of Cr (5.1 kg) and Sr (-10.8 kg) in the upper meter of profile (nodular bauxite) (see Tab DR4b).

## 5. Discussion

### 5.1. Differential bauxitic weathering and chemical erosion of volcanic rocks

The two bauxitic duricrusted profiles show different weathering and geochemical paths from saprolite to lateritic duricrusted horizons. Owing to strong leaching of silica and alkaline/alkaline earth elements, intense lateritization process resulted in gibbsite replacement of

**Table 1**

Variations of bulk and grain density ( $\rho_b$  and  $\rho_g$  in  $\text{g}\cdot\text{cm}^{-3}$ ), porosity,  $\phi$ , strain,  $\epsilon$ , and elements transfer rates,  $\tau$ , in weathering profiles formed upon (a) trachyte ( $\epsilon$  calculated with reference element Zr), and (b) basalt ( $\epsilon$  calculated with reference element Ti). Calculated from the equations (1) to (3), respectively. The true depth of trachyte being unknown we simply mentioned a depth in parentheses for graphical easiness of figures.

(a)	Horizon	Depth (m)	$\rho_b$	$\rho_g$	$\phi$	$\epsilon_{Zr}$	$\tau_{Si}$	$\tau_{Al}$	$\tau_{Fe}$	$\tau_{Ti}$	$\tau_{Ca}$	$\tau_{Mg}$	$\tau_{Na}$	$\tau_K$	$\tau_{Mn}$	$\tau_P$
P2-FO-2	B3	2.50	1.73	2.28	24.0	-0,48	-0,99	0,17	-0,40	0,32	-1,00	-0,98	-1,00	-1,00	-0,95	-0,27
P2-FO-3	B3	4.50	1.93	2.50	22.7	-0,68	-1,00	-0,30	-0,26	0,36	-1,00	-1,00	-1,00	-1,00	-0,96	-0,46
P2-FO-4	B3	6.00	1.90	2.32	18.4	-0,54	-1,00	0,09	-0,16	0,21	-1,00	-1,00	-1,00	-1,00	-0,96	-0,44
P2-FO-5	B3	8.00	1.69	2.47	31.7	-0,65	-1,00	-0,33	-0,30	0,27	-0,99	-1,00	-1,00	-1,00	-0,96	-0,44
P2-FO-6	B3	9.00	1.87	2.43	23.3	-0,50	-0,99	0,22	-0,24	0,26	-1,00	-1,00	-1,00	-1,00	-0,92	-0,63
P2-FO-7	B3	10.0	1.83	2.35	22	-0,44	-0,99	0,35	-0,16	0,33	-1,00	-1,00	-1,00	-1,00	-0,92	-0,32
P2-FO-7.1	B3	10.5	2.76	2.82	2.06	-0,30	-0,98	0,17	0,97	0,36	-1,00	-1,00	-1,00	-1,00	-0,67	1,55
P2-FO-8	B5	11.0	1.74	2.46	29.2	-0,46	-0,99	0,19	-0,10	0,56	-1,00	-1,00	-1,00	-1,00	-0,93	-0,42
P2-FO-8.1	B5	11.5	1.64	2.42	32.3	-0,49	-0,97	-0,16	0,03	0,52	-0,99	-0,91	-1,00	-1,00	-0,91	-0,15
P3-FO-3	C	12.0	1.41	2.04	30.9	-0,55	-0,89	-0,44	-0,48	0,35	-1,00	-0,99	-1,00	-1,00	-0,95	-0,14
Trachyte		(13.0)	2.53	2.55	0.78	0,00	0,00	0,00	0,00	0,00	0,00	0,00	0,00	0,00	0,00	0,00
<b>(b)</b>						$\epsilon_{Ti}$										
P1-SA	B2	1.00	2.33	2.58	9.69	0,14	-0,78	1,68	0,90		-1,00	-0,99	-1,00	-0,98	-0,83	-0,50
P1-SA-2	B3	4.00	2.06	2.78	25.9	-0,39	-0,98	0,25	0,10		-1,00	-0,99	-1,00	-1,00	-0,88	-0,91
P1-SA-3	B4	6.50	1.36	2.21	38.6	0,00	-0,76	0,05	-0,08		-1,00	-0,98	-1,00	-0,98	-0,74	-0,80
P1-SA-4	B4	8.00	1.66	2.51	34	-0,31	-0,84	-0,16	-0,16		-1,00	-0,97	-1,00	-1,00	-0,78	-0,49
P1-SA-5	C	9.50	1.38	2.25	38.8	0,21	-0,58	0,06	-0,08		-0,99	-0,91	-1,00	-0,95	-0,44	-0,42
Basalt		10.5	2.74	2.74	0.0	0,00	0,00	0,00	0,00		0,00	0,00	0,00	0,00	0,00	0,00

kaolinite and formation of iron oxy-hydroxides (goethite and hematite) under redox conditions favorable to Al and Fe concentration (see Beauvais and Colin, 1993; Schellmann, 1994; Eggleton et al., 2008; Beauvais, 2009), which are illustrated by secondary gibbsite crystallizations, and clay-Fe coatings or cutans (Fig. 5b and 5d; see also Momo Nouazi et al., 2019).

Element mass transfers point out important Al and Fe concentrations in the profile formed on basalt, while Al and Fe were seemingly exported from some bauxitic horizons of the profile formed on trachyte (Tab. 2 and Fig. 10) correlatively to the anomalous increase in reference elements Zr and Ti in these horizons (see Fig. 7c-d, Fig. 8 and Table DR2a). Enrichment of Zr and Ti, along with irregular Zr/Ti ratios during formation of trachyte profile may owe to their heterogeneity in the fresh trachyte (Brimhall et al., 1991; Schwarz, 1997). Mechanical reworking of weathering-resistant carrier heavy minerals (zircon, ilmenite and rutile) may also occur during long-term complex evolution of lateritic profiles (e.g., Brimhall et al., 1991; Colin et al., 1992; see also Beauvais, 2009). Given translocation marks in many lateritic weathering profiles (e.g., Fig. 5d), physical release of small size fractions of Zr and Ti carrier minerals (mostly zircon and titanomagnetite), which migrated downward into the compacted residual weathering profile, was also previously observed (e.g., Fig. 5d; see also Schwarz, 1997; Brimhall et al., 1988, 1991; Colin et al., 1992). Hence, this complex and

differential behavior of Zr and Ti during the formation and evolution of residual lateritic profiles has resulted in differential strains implying the chemical weathering of protoliths (parent-rocks) of different thickness (see Eq. (5)).

Given the ages of parent rocks (16 Ma for trachyte and 14 Ma for basalt), quantification of their initial thickness before onset of weathering that produced the lateritic profiles allows estimating average minimum rates of rock chemical erosion over the Neogene. Upon basalt, calculations with Ti give an integrated chemical rock-weathering rate of ca. 0.84 m/my over the last 14 Myr. A basalt thickness of ca. 12 m is required to produce the investigated residual ca. 10 m thick weathering profile at a rate of 0.70 m/my. This also implies a topographic erosion of only ca. 2 m owing to congruent rock chemical erosion at a rate of ca. 0.14 m/my during the same period that is consistent with an almost isovolumetric basalt weathering (average  $\epsilon_{Ti,w} = -0,07$ ; Tab. 1). Congruent chemical weathering of 2 m<sup>3</sup> thick basalt ( $\rho = 2.74 \text{ t/m}^3$ ) corresponds to net exports of ca. 1076 kg Si, 377 kg Al and 546 kg Fe. Upon trachyte, calculations with Zr give an integrated chemical rock-weathering rate of c. 1.625 m/my. Here, chemical weathering of ca. 26 m thick trachyte led to formation of the 12 m thick studied profile consistently with an average strain value of  $\epsilon_{Zr,w} = -0,51$  (Tab. 1). This implies a topographic decay of similar height of 14 m corresponding to the thickness of rock layer, which has been chemically

**Table 2**

Elements mass transfers in kg per unit volume (1 m<sup>3</sup>) in weathering profiles formed on (a) trachyte and (b) basalt. Calculated from the equation (4).

(a)	Horizon	Depth (m)	$m_{Si}$	$m_{Al}$	$m_{Fe}$	$m_{Ti}$	$m_{Ca}$	$m_{Mg}$	$m_{Na}$	$m_K$	$m_{Mn}$	$m_P$
P2-FO-2	B3	2.5	-695.3	34.6	-58.8	3.0	-51.5	-3.2	-81.7	-106.5	-7.2	-0.5
P2-FO-3	B3	4.5	-700.4	-62.4	-39.1	3.3	-51.4	-3.3	-81.7	-106.7	-7.3	-0.8
P2-FO-4	B3	6.0	-700.6	18.3	-24.4	1.9	-51.5	-3.3	-81.7	-106.7	-7.3	-0.8
P2-FO-5	B3	8.0	-701.4	-68.0	-44.1	2.6	-51.3	-3.3	-81.7	-106.7	-7.3	-0.8
P2-FO-6	B3	9.0	-695.8	45.8	-35.4	2.4	-51.5	-3.3	-81.7	-106.7	-6.9	-1.1
P2-FO-7	B3	10.0	-697.3	72.2	-24.2	3.1	-51.5	-3.3	-81.7	-106.7	-7.0	-0.6
P2-FO-7.1	B3	10.5	-688.7	35.4	144.3	3.4	-51.5	-3.3	-81.7	-106.6	-5.1	2.7
P2-FO-8	B5	11.0	-696.6	39.9	-15.1	5.3	-51.6	-3.3	-81.7	-106.6	-7.1	-0.7
P2-FO-8.1	B5	11.5	-680.6	-32.8	4.1	4.9	-51.2	-3.0	-81.7	-106.3	-6.9	-0.3
P3-FO-3	C	12.0	-625.3	-92.3	-72.0	3.3	-51.4	-3.2	-81.7	-106.7	-7.2	-0.2
Trachyte		(13.0)	0.00	0.00	0.00	0.00	0.00	0.00	0.00	0.00	0.00	0.00
<b>(b)</b>												
P1-SA	B2	1.0	-421.7	316.6	246.0		-177.2	-182.8	-42.7	-21.2	-4.1	-3.3
P1-SA-2	B3	4.0	-527.4	46.4	28.5		-177.5	-183.1	-42.7	-21.7	-4.3	-5.9
P1-SA-3	B4	6.5	-408.0	9.6	-22.7		-177.1	-180.7	-42.7	-21.2	-3.7	-5.3
P1-SA-4	B4	8.0	-453.1	-29.8	-43.5		-176.9	-179.5	-42.7	-21.6	-3.9	-3.2
P1-SA-5	C	9.5	-313.7	10.8	-22.5		-176.4	-168.6	-42.7	-20.5	-2.2	-2.8
Basalt		10.5	0.0	0.0	0.0		0.0	0.0	0.0	0.0	0.0	0.0

**Table 3**

Transferred masses of elements integrated over the investigated profile horizons thickness ( $\Delta Z_w$ ), related to the corresponding height or thickness of chemically weathered rock layer ( $\Delta Z$ ), in profile on a) trachyte, and b) basalt. Calculated from the equation (5).

(a)	Horizon	Depth (m)	$\Delta Z$ (m)	$\Delta Z_w$ (m)	$M_{Si}$	$M_{Al}$	$M_{Fe}$	$M_{Ti}$	$M_{Ca}$	$M_{Mg}$	$M_{Na}$	$M_K$	$M_{Mn}$	$M_P$
P2-FO-2	B3	2.5	4.8	2.5	-3349	167	-283	15	-248	-16	-394	-513	-35	-2
P2-FO-3	B3	4.5	3.1	1.0	-2165	-193	-121	10	-159	-10	-253	-330	-23	-3
P2-FO-4	B3	6.0	6.0	2.75	-4216	110	-147	12	-310	-20	-492	-642	-44	-5
P2-FO-5	B3	8.0	2.9	1.00	-2017	-196	-127	7	-147	-9	-235	-307	-21	-2
P2-FO-6	B3	9.0	2.5	1.25	-1747	115	-89	6	-129	-8	-205	-268	-17	-3
P2-FO-7	B3	10.0	1.3	0.75	-937	97	-33	4	-69	-4	-110	-143	-9	-1
P2-FO-7.1	B3	10.5	0.7	0.50	-495	25	104	2	-37	-2	-59	-77	-4	2
P2-FO-8	B5	11.0	0.9	0.50	-641	37	-14	5	-48	-3	-75	-98	-7	-1
P2-FO-8.1	B5	11.5	0.5	0.25	-331	-16	2	2	-25	-1	-40	-52	-3	0
P3-FO-3	C	12.0	3.3	1.50	-2084	-308	-240	11	-171	-11	-272	-356	-24	-1
Trachyte		(13.0)	26.0		0	0	0	0	0	0	0	0	0	0
<b>(b)</b>														
P1-SA	B2	1.0	1.3	1.50	-556	417	324		-234	-241	-56	-28	-5	-4
P1-SA-2	B3	4.0	6.0	3.70	-3188	281	172		-1073	-1107	-258	-131	-26	-36
P1-SA-3	B4	6.5	1.5	1.55	-630	15	-35		-274	-279	-66	-33	-6	-8
P1-SA-4	B4	8.0	1.1	0.75	-492	-32	-47		-192	-195	-46	-24	-4	-4
P1-SA-5	C	9.5	1.8	2.20	-570	20	-41		-321	-306	-78	-37	-4	-5
Basalt		10.5	12.0		0	0	0		0	0	0	0	0	0

eroded congruently over the last 16 Myr at a rate of 0.875 m/my, while the residual weathering profile formed at rate of ca. 0.75 m/my that is comparable with the rate of profile formation upon the basalt. Upon formation of the 12 m thick lateritic profile, the congruent chemical erosion of 14 m<sup>3</sup> trachyte ( $\rho = 2.53 \text{ t/m}^3$ ) resulted in net exports of ca. 9849 kg Si, 2904 kg Al and 2083 kg Fe.

Therefore, differential chemical erosion of trachyte and basalt is

primarily dependent on differences of strain ( $\epsilon_{i,w}$ ) in profiles (Egli et Fitze, 2000). This implies formation of an equal 1 m thick bauxitic profile from the chemical weathering of a ca. 2.2 m thick layer of trachyte against 1.2 m thick basalt layer over 1 My and 1.8 My, respectively. However, such differences call further discussion on parent-rocks geochemical differences and potential geomorphological constraints.

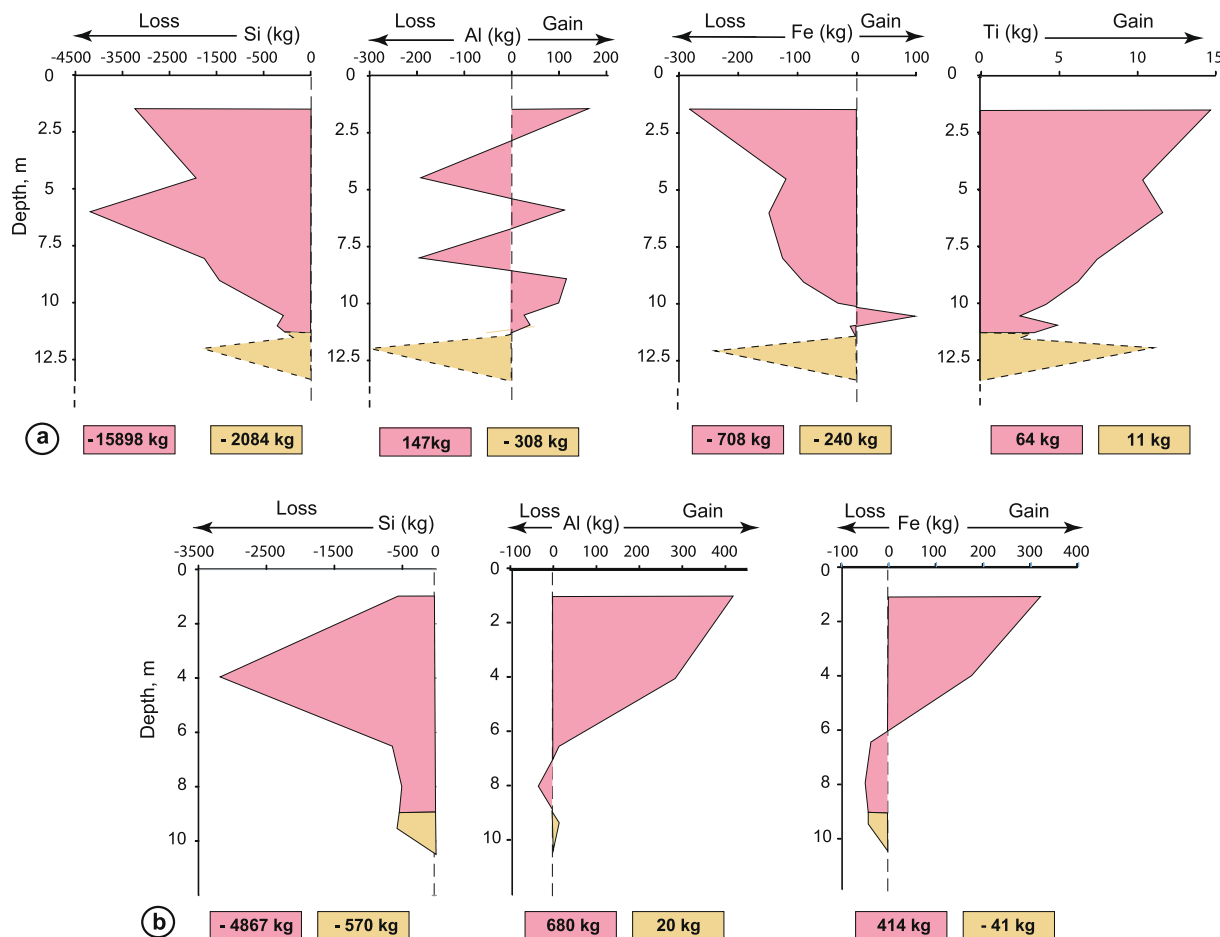


**Fig. 10.** Comparative transferred masses of major elements over integrated thicknesses of protolith layers chemically weathered to form the saprolite (yellow) and bauxitic duricrusted horizons (pink) in the weathering profile formed on a) trachyte and b) basalt. (Masses calculated from equation (5); see also Table 3). (For interpretation of the references to colour in this figure legend, the reader is referred to the web version of this article.)

## 5.2. Constraints to differentiated bauxitic weathering in highland western Cameroon

Under similar climatic and floristic constraints, differential chemical erosion and bauxitic weathering potentially depend on parent rocks composition differences, but also from drainage constraints upon profiles and landscape owing to local differential tectonics related to the volcanic dynamics of Cameroon.

Although olivines are known to be more weathering-reactive than plagioclase and pyroxenes (Eggleton et al., 1987; Schwarz, 1997), these minerals present grossly similar weathering rates (Nesbitt and Wilson, 1992), no matter the grain size (Israeli and Emmanuel, 2018). This suggests no direct (or little) influence of differential mineral sensitivity on weathering rates and geochemical transfers on different volcanic rocks. Nonetheless, Basalt carry mainly Fe-Mg minerals (olivine and clinopyroxene), while trachyte are mostly Si-Al rich with dominant plagioclases and pyroxenes. However, the total mass of Si released during rock weathering and formation of evolved bauxitic profiles (sum of element masses exported as synthesized in Fig. 10) is a few more than thrice on Si-rich trachyte than on basalt (17982 kg against 5437 kg), whose the lateritic bauxitic profile has accumulated a few four time more Al than on trachyte (Tab. 3b and Fig. 10b).

According to Braun et al. (2016), chemical weathering rate is primarily controlled by groundwater capacity to export solutes (e.g., dissolved silica, see also Schopka and Derry, 2012) far from the reacting solid–fluid interface to impede saturation of the weathering system. This requires continuous and efficient drainage to sustaining propagation of the weathering front into the bedrock (Braun et al., 2012; Prestrud Anderson et al., 2007, and references there-in). Weathering in profile on trachyte may have been enhanced by interconnected porosity (Momo Nouazi et al., 2019) that was formed by eluviation process of less cohesive clayey matrix (Fig. 5a). On the other hand, compact and Fe-coated clay matrix upon basalt has slowed rock weathering (Fig. 5c). This resulted here in rates lower than overall estimates in different geological and climatic contexts (Australia, Northern and Southern America; see Stockmann et al., 2014), despite high alterability of basalt.

However, rock-weathering rates, geochemical transfers and residual profile growth are primarily dependent on silica content of parent rock to be exported by groundwater to streams (Schopka and Derry, 2012). Higher Si abundance in trachyte relative to basalt (Figs. 4 and 6) is thus a major geochemical constraint to the growth of weathering profiles. Optimal drainage upon weathering front was instrumental for rapid dissolution of abundant Si carrier minerals (plagioclases) in trachyte, which turned into weathering rate-controlling minerals. A volcanic-related tectonic instability during Miocene (and later) has potentially led to rapid deepening of base level and landscape incision in Mount Bambouto (location in Fig. 2; see also Figs. DR1-a-b). This resulted in landscape rejuvenation, and optimal drainage that sustained eluviation processes in soils and weathering profiles, thus favoring silica export. Hence, saprolite production rate has been higher on trachyte than on basalt extruded at lower altitude, and where lateritic plateaus are less incised further away from tectonic influences (e.g., Prestrud Anderson et al., 2007; Brantley et al., 2007; Schopka and Derry, 2012). Furthermore, differences in geomorphic processes resulted in differential evolution of profiles over Neogene, with an almost iso-volumetric formation on basalt ( $\epsilon_{Ti,w} = -0,07$ ), while the profile on trachyte underwent a substantial collapse ( $\epsilon_{Zr,w} = -0,51$ ).

Therefore, geochemical differences in volcanic rocks compositions (mostly silica content) and geomorphological constraints potentially controlled by differential tectonics have resulted together in differentiation of chemical erosion and bauxitic weathering in highland western Cameroon (see also Samonil et al., 2020). The current bauxitic plateaus stand as long-lived elevated but differentially incised landforms (Figs. DR1a-b; see also Momo Nouazi et al., 2016). This implies the protolith-regolith interface has seemingly moved downward non-

uniformly with respect to differentially eroded/incised geomorphic surfaces on trachyte and basalt over the last 15 My.

## 6. Conclusion

Comparative geochemical mass balances of lateritic weathering of Mid-Miocene aged trachyte and basalt in highland western Cameroon document different processes of chemical erosion and weathering profile formation. Reference elements Zr and Ti have been used from their relative stability for calculating element mass transfers in weathering profiles. Despite some geochemical anomalies in Zr or Ti owing to possible heterogeneity in parent photoliths and physical enrichments of carrier heavy minerals in residual profiles, element mass transfers indicate higher Si depletion and lower Al-Fe concentrations on trachyte than on basalt. Our results document the formation of 1 m thick bauxitic profile from lateritic weathering of 1.2 m of basalt or 2.2 m of trachyte, implying chemical erosion and weathering rates lower on basalt than on trachyte. Different strain pattern in the investigated weathering profiles imply a congruent dissolution (net chemical erosion) of initial protolith layer larger on trachyte (14 m) than on basalt (2 m). Differential chemical weathering rates are mostly controlled by drainage conditions at the regolith-photolith interface and the Si content of volcanic rocks to be released to form bauxitic regolith. Finally, our results point out combined influence of differential local tectonics, and geochemical differences of volcanic rocks on chemical erosion and bauxitic weathering, with implications on the evolution of western Cameroon landscapes over the Neogene.

## Acknowledgments

Financial support was provided by the ‘Service de Coopération et d’Action Culturelle au Cameroun (SCAC)’ from the French Embassy (791779A). The mineralogical analyses have been carried out at the Centre Européen de Recherche et d’Enseignement des Géosciences de l’Environnement (CEREGE), Aix Marseille University, OSU Pytheas, France. The geochemical analysis has been carried out at ALS Laboratory Group SL-Spain. MNM was supported by a 6 months fellowship from the ‘Institute of Research for Development’ (IRD, France). We acknowledge Dr. Nkouathio for geochronological data and assistance on volcanic model of the mount Bambouto. Jean Paul Ambrosi is thanked for technical assistance and discussion of some results. We are grateful to Dr. R.A. Eggleton, an anonymous reviewer, and Pr. Egli, for their respective remarks and suggestions that together contributed to clarify and improve our manuscript.

## Appendix A. Supplementary material

Supplementary data to this article can be found online at <https://doi.org/10.1016/j.catena.2020.104685>.

## References

- American Mineralogist Crystal Structure Database. <http://rruff.geo.arizona.edu/AMS/amcsd.php>. Accessed date: 8 June 2017.
- Babechuk, M.G., Widdowson, M., Kamber, B.S., 2014. Quantifying chemical intensity and trace element release from two contrasting profiles, Decan Traps India. *Chem. Geol.* 365, 56–75.
- Babechuk, M.G., Widdowson, M., Murphy, M., Kamber, B.S., 2015. A combined Y/Ho, high field strength element (HFSE) and Nd isotope perspective on basalt weathering, Deccan Traps, India. *Chem. Geol.* 396, 25–41.
- Bardossy, G.Y., Aleva, G.J.J., 1990. Lateritic bauxites. Elsevier, Amsterdam, pp. 624.
- Beauvais, A., 2009. Ferricrete biochemical degradation on the rainforest savannas boundary of Central African Republic. *Geoderma* 150, 379–388.
- Beauvais, A., Colin, F., 1993. Formation and transformation processes of iron duricrust systems in tropical humid environment. *Chem. Geol.* 106, 77–151.
- Beauvais, A., Chardon, D., 2013. Modes, tempo, and spatial variability of Cenozoic tectonic erosion: the West African example. *Geochem. Geophys. Geosyst.* 14, 1590–1608. <https://doi.org/10.1002/ggge.20093>.

- Beauvais, A., Ruffet, G., Hénocque, O., Colin, F., 2008. Chemical and physical erosion rhythms of the West African Cenozoic morphogenesis: The  $^{39}\text{Ar}$ - $^{40}\text{Ar}$  dating of supergene K-Mn oxides. *J. Geophys. Res.* 113, F04007. <https://doi.org/10.1029/2008JF000996>.
- Boulangé, B., Millot, G., 1988. La distribution des bauxites sur le craton ouest-africain. *Sci. Géol. Bull.* 41, 113–123.
- Boulangé, B., 1984. Les formations bauxitiques latéritiques de Côte d'Ivoire. Les faciès, leur transformation, leur distribution et l'évolution du modelé. In: Thèse et Mémoire ORSTOM 363 pp.
- Boulangé, B., Colin, F., 1994. Rare earth element mobility during conversion of nepheline syenite into lateritic bauxite at Passa Quatro, Minas Gerais, Brazil. *Appl. Geochem.* 9, 701–711.
- Brantley, S.L., Goldhaber, M.B., Ragnarsdottir, K.V., 2007. Crossing disciplines and scales to understand the critical zone. *Elements* 3, 307–314.
- Brantley, S.L., Lebedeva, M., 2011. Learning to read the chemistry of regolith to understand the critical zone. *Ann. Rev. Earth Planetary Sci.* 39, 387–416.
- Braun, J.J., Mercier, J., Guillocheau, F., Robin, C., 2016. A simple model for regolith formation by chemical weathering. *J. Geophys. Res. Earth Surf.* 121, 2140–2171. <https://doi.org/10.1002/2016JF003914>.
- Braun, J.J., Pagel, M., Herbillon, A., Rosin, C., 1993. Mobilization and redistribution of REEs and thorium in syenitic lateritic profile: A mass balance study. *Geochim. Cosmochim. Acta* 57, 4419–4434.
- Braun, J.J., Marechal, J.C., Riotte, J., Boeglin, J.L., Bedimo Bedimo, J.P., Ndam Ngoupayou, J.R., Nyeck, B., Robain, H., Sekhar, M., Audry, S., Viers, J., 2012. Elemental weathering fluxes and saprolite production rate in a Central African lateritic terrain (Nsimi, South Cameroon). *Geochim. Cosmochim. Acta* 99, 243–270.
- Brimhall, G.H., Dietrich, W.E., 1987. Constitutive mass balance relations between chemical composition, volume, density, porosity, and strain in metasomatic hydrochemical systems: Results on weathering and pedogenesis. *Geochim. Cosmochim. Acta* 51, 567–587.
- Brimhall, G.H., Lewis, C.J., Ague, J.J., Dietrich, W.E., Hampel, J., Teague, T., Rix, P., 1988. Metal enrichment in bauxites by deposition of chemically mature aeolian dust. *Nature* 333, 819–824.
- Brimhall, G.H., Lewis, C.J., Ford, C., Bratt, J., Taylor, G., Warin, O., 1991. Quantitative geochemical approach to pedogenesis: importance of parent material reduction, volumetric expansion and eolian influx on lateritization. *Geoderma* 51, 51–91.
- Burke, K., Gunnell, Y., 2008. The African Erosion Surface: A Continental-Scale Synthesis of Geomorphology, Tectonics, and Environmental Change over the Past 180 Million Year. *Geological Society of America, Memoir* 201, 66 p.
- Chadwick, O.A., Brimhall, G.H., Hendricks, D.M., 1990. From a black to a gray box-A mass balance interpretation of pedogenesis. *Geomorphology* 3, 369–390.
- Chardon, D., Grimaud, J.L., Beauvais, A., Bamba, O., 2018. West African lateritic pediments: Landform-regolith evolution processes and mineral exploration pitfalls. *Earth-Sci. Rev.* 179, 124–146.
- Colin, F., Brimhall, G.H., Nahon, D., Baronnet, A., Kathy, D., 1992. Equatorial rainforest lateritic mantles: a geomembrane filter. *Geology* 20, 523–526.
- De Putter, T., Ruffet, G., 2020. Supergene manganese ore records 75 Myr-long Campanian to Pleistocene geodynamic evolution and weathering history of the Central African Great Lakes Region - Tectonics drives, climate assists. *Gondwana Res.* 83, 96–117.
- Déruelle, B., Ngounou, I., Demaiffe, D., 2007. The 'Cameroon Hot Line' (CHL): a unique example of active alkaline intraplate. structure in both oceanic and continental lithospheres. *C.R. Geoscience* 339, 589–600.
- Eggleton, R.A., Taylor, G., Le Gleuher, M., Foster, L.D., Tilley, D.B., Morgan, C.M., 2008. Regolith profile, mineralogy and geochemistry of the Weipa Bauxite, northern Australia. *Aust. J. Earth Sci.* 55, 17–43. <https://doi.org/10.1080/08120090802438233>.
- Eggleton, R.A., Foudoulis, C., Varkevissar, D., 1987. Weathering of basalt: changes in rock chemistry and mineralogy. *Clays Clay Miner.* 35 (3), 161–169.
- Egli, M., Fitze, P., 2000. Formulation of pedologic mass balance based on immobile elements: a revision. *Soil Sci.* 165, 437–443.
- Fosso, J., Ménard, J.J., Bardintzeff, J.M., Wandji, P., Tchoua, F.M., Bellon, H., 2005. Les laves du mont Bangou : une première manifestation volcanique éocène, à affinité transitionnelle, de la Ligne du Cameroun. *C.R. Geosciences* 337, 315–325.
- Israeli, Y., Emmanuel, S., 2018. Impact of grain size and rock composition on simulated rock weathering. *Earth Surf. Dyn.* 6, 319–327.
- Jean, A., Beauvais, A., Chardon, D., Arnaud, N., Jayanada M., Mathe, P. E., 2020. Weathering history and landscape evolution of Western Ghats (India) from  $^{40}\text{Ar}/^{39}\text{Ar}$  dating of supergene K-Mn oxides. *Journal of the Geological Society, London*. In press, doi: 10.1144/jgs2019-048.
- Kengni, L., Tekoudjou, H., Tematio, P., Tedonkeng, E.P., Mubeteneh Tankou, C., 2009. Rainfall Variability along the Southern Flank of the Bambouto Mountain (West-Cameroon). *J. Cameroon Academy Sci.* 8, 45–52.
- Kwékam, M., Liégeois, J.P., Njonfang, E., Affaton, P., Hartmann, G., 2010. Nature, origin and significance of the Pomopéa Pan-African high-K calc-alkaline plutonic complex in the Central African fold belt (Cameroon). *J. Afr. Earth Sc.* 57, 79–95.
- Marzoli, A., Piccirillo, E.M., Renne, P.R., Bellieni, G., Iacumin, M., Nyobe, J.B., Tongwa, A.T., 2000. The Cameroon Volcanic Line revisited: Petrogenesis of continental basaltic magmas from lithospheric and asthenospheric mantle sources. *J. Petrol.* 41, 87–109.
- Marzoli, A., Renne, P. R., Piccirillo, E. M., Francesca, C., Bellieni, G., Mel, A. J., Nyobe, J. B., N'ni, J., 1999. Silicic magmas from the continental Cameroon Volcanic Line (Oku, Bambouto and Ngaoundéré):  $^{40}\text{Ar}/^{39}\text{Ar}$  dates, petrology, Sr-Nd-O isotopes and their petrogenetic significance. *Contrib Mineral Petrol* 135, 133–150.
- Millot, G., Bonifas, M., 1959. Transformations isovolumétriques dans les phénomènes de latérisation et de bauxitisation. *Bull. Serv. Carte Géol. Alsace. Lorraine* 8, 3–10.
- Momo Nouazi, M., Beauvais, A., Tematio, P., Ambrosi, J.-P., Yemefack, M., Yerima, P.K.B., Yongue-Fouateu, R., 2019. Lateritic weathering of trachyte, and bauxite formation in West Cameroon: Morphological and geochemical evolution. *J. Geochem. Explor.* 205, 106324. <https://doi.org/10.1016/j.gexplo.2019.06.006>.
- Momo Nouazi, M., Yemefack, M., Tematio, P., Beauvais, A., Ambrosi, J.-P., 2016. Distribution of duricrusted bauxites and laterites on the Bamiléké plateau (West Cameroon): Constraints from GIS mapping and geochemistry. *Catena* 140, 15–23.
- Moundi, A., Wandji, P., Bardintzeff, J.M., Ménard, J.J., Okomo Atouba, L.C., Mouncherou, O.F., Reusser, E., Bellon, H., Tchoua, F.M., 2007. Les basaltes éocènes à affinité transitionnelle du plateau Bamoun, témoins d'un réservoir mantellique enrichi sous la Ligne Volcanique du Cameroun. *C.R. Geosciences* 339, 396–406.
- Nesbitt, H.W., Wilson, R.E., 1992. Recent chemical weathering of basalt. *Am. J. Sci.* 292, 740–777.
- Nkouathio, D.G., Kagou Dongmo, A., Bardintzeff, J.M., Wandji, P., Bellon, H., Poulet, A., 2008. Evolution of volcanism in graben and horst structures along the Cenozoic Cameroon Line (Africa): implications for tectonic evolution and mantle source composition. *Mineral. Petrol.* 94, 287–303.
- Perelló, J., Brockway, H., Garcia, A., 2020. A minimum Thanetian (Paleocene) age for the African Surface in the Eritrean highlands, Northeast Africa. *J. Afr. Earth Sc.* 164, 103782.
- Prestrud Anderson, S., Von Blanckenburg, F., White, A.F., 2007. Physical and chemical control on the critical zone. *Elements* 3, 315–319.
- Retallack, G.J., 2010. Lateritization and Bauxitization Events. *Econ. Geol.* 105, 655–667.
- Rietveld, H.M., 1969. A profile refinement method for nuclear and magnetic structures. *J. Appl. Crystallogr.* 2, 65–71.
- Samonil, P., Philipps, J., Danek, P., Benes, V., Pawlik, L., 2020. Soil, regolith, and weathered rock: Theoretical concepts and evolution in old-growth temperate forests. *Central Europe. Geoderma* 368, 114261. <https://doi.org/10.1016/j.geoderma.2020.114261>.
- Schellmann, W., 1994. Geochemical differentiation in laterite and bauxite formation. In *Lateritization Processes and Supergene Ore Formation. Catena Spec. Issue* (eds T. Schwarz and K. Germann), 21, 141–143. Elsevier.
- Schopka, H.H., Derry, L.A., 2012. Chemical weathering fluxes from volcanic islands and the importance of groundwater: The Hawaiian example. *Earth Planet. Sci. Lett.* 339–340, 67–78.
- Schwarz, T., 1997. Distribution and genesis of bauxite on the Mambilla plateau. *SE Nigeria. Applied Geochemistry* 12, 119–131.
- Soares de Oliveira, F., Chicarino Varajão, A.F.D., Chicarino Varajão, C.A., Boulangé, B., Vieira Soares, C.C., 2013. Mineralogical, micromorphological and geochemical evolution of the facies from the bauxite deposit of Barro Alto, Central Brazil. *Catena* 105, 29–39.
- Soler, J.M., Lasaga, A.C., 2000. The Los Pijiguas bauxite deposit (Venezuela): A compilation of field data and implications for the bauxitization process. *J. S. Am. Earth Sci.* 13, 47–65.
- Stockmann, U., Minasny, B., McBratney, A.B., 2014. How fast does soil grow? *Geoderma* 216, 48–61.
- Tardy, Y., 1997. Petrology of Laterites and Tropical Soils. Balkema, Rotterdam, pp. 408.
- Tematio, P., Fritsch, E., Hodson, M.E., Lucas, Y., Bitom, D., Bilong, P., 2009. Mineral and geochemical characterization of a leptic aluandic soil and a thapto aluandic-ferralsol developed on trachyte in Mount Bambouto (Cameroon volcanic line). *Geoderma* 152, 314–323.
- Tematio, P., Olson, K.R., 1997. Characterization of two phases of encrustment in a sequence of ferrallitic soils in the South Cameroon and its effects on landscape evolution. *Soil Sci.* 162 (10), 758–766.
- Temgoua, E., Pfeiffer, H.-R., Bitom, D., 2003. Trace element differentiation in ferruginous accumulation soil patterns under tropical rainforest of southern Cameroon, the role of climatic change. *The Science of the Total Environment* 303, 203–214.
- Thomas, M.F., 1994. Geomorphology in the tropics: a study of weathering and denudation in low altitudes. John Wiley and Sons, Chichester, pp. 460.
- Ufer, K., Stanjek, H., Roth, G., Dohrmann, R., Kleeberg, R., Kaufhold, S., 2008. Quantitative phase analysis of bentonites by the Rietveld method. *Clay Clay Miner.* 56 (2), 272–282.
- Valeton, I., 1999. Saprolite-bauxite facies of ferrallitic duricrusts on palaeosurfaces of former Pangea. *Sp. Pub. Int. Ass. Sedim.* 27, 153–188.
- Valeton, I., Beißner, H., 1986. Geochemistry and mineralogy of the lower tertiary in situ laterites of the Jos plateau. *Journal of African Earth Sciences* 5, 535–550.
- Wille, M., Babechuk, M.G., Kleinhans, I.C., Steigmaier, C., Suhr, N., Widdowson, M., Kamber, B.S., Shoenberg, R., 2018. Silicon and chromium stable isotopic systematics during basalt weathering and lateritisation: A comparison of variably weathered basalt profiles in the Deccan Traps, India. *Geoderma* 314, 190–204.
- White, A.F., Bullen, T.D., Schultz, M.S., Blum, A.E., Huntington, T.G., Peters, N.E., 2001. Differential rates of feldspar weathering in granitic regoliths. *Geochim. Cosmochim. Acta* 65, 847–869.
- Zarasvandi, A., Carranza, E.J.M., Ellahi, S.S., 2012. Geological, geochemical and mineralogical characteristics of the Deh-Now bauxite deposits, Zagros fold belt. *Iran. Ore Geol. Rev.* 48, 125–138.